Combustion synthesis of metal carbides: Part II. Numerical simulation and comparison with experimental data

A.M. Locci, A. Cincotti[a], F. Delogu, and R. Orrù
Dipartimento di Ingegneria Chimica e Materiali, Centro Studi sulle Reazioni Autopropaganti (CESRA), Unità di Ricerca del Consorzio Interuniversitario Nazionale di Scienza e Tecnologia dei Materiali (INSTM), Università degli Studi di Cagliari, Piazza d'Armi, 09123 Cagliari, Italy

G. Cao[b]
Dipartimento di Ingegneria Chimica e Materiali, Centro Studi sulle Reazioni Autopropaganti (CESRA), Unità di Ricerca del Consorzio Interuniversitario Nazionale di Scienza e Tecnologia dei Materiali (INSTM), Università degli Studi di Cagliari, Piazza d'Armi, 09123 Cagliari, Italy, and CRS4, Parco Scientifico e Tecnologico, POLARIS, Edificio 1, 09010 Pula (CA), Italy

(Received 15 October 2004; accepted 8 February 2005)

Based on the general theoretical model proposed in Part I of this work [J. Mater. Res. **20,** 1257 (2005)], a series of numerical simulations related to the self-propagating high-temperature synthesis in the Ti–C system is presented. A detailed and quantitative description of the various physical and chemical processes that take place during combustion synthesis processes is provided in Part II of this work. In particular, the proposed mathematical description of the system has been discussed by highlighting the relation between system macroscopic behavior obtained experimentally with the modeled phenomena taking place at the microscopic scale. Model reliability is tested by comparison with suitable experimental data being nucleation parameters adopted for the fitting procedure. The complex picture emerging as a result of the model sophistication indicates that the rate of conversion is essentially determined by the rate of nucleation and growth. In addition, comparison between model results and experimental data seems to confirm the occurrence of heterogeneous nucleation in product crystallization.

I. INTRODUCTION

Self-propagating high-temperature synthesis (SHS) processes have been widely investigated to prepare a large number of advanced ceramic, intermetallic, and composite materials.[1] It is well known that SHS may be regarded as a complex process involving several interrelated phenomena such as the formation of molten phases as well as of final solid products and their subsequent microstructural evolution. Consequently, degree of sophistication of the mathematical description of SHS may be considerably high.[2,3]

As discussed in Part I of this work,[4] several homogeneous and heterogeneous approaches have been adopted for modeling important features of SHS processes.[5–9] However, since a comprehensive description of all the complex phenomena taking place was still missing, a novel mathematical model to thoroughly simulate SHS processes is proposed in Part I of this work.[4] Based on a heterogeneous approach first presented by Stangle and co-workers,[10–12] the proposed model simulates microstructural evolution using suitable population balances and properly evaluating the different driving forces from the relevant phase diagram. The main goal of this long-term approach is to establish an advanced modeling strategy for SHS processes, which not only provides a proper tool for design of suitable reactors but will also serve as a diagnostic medium for the quantitative interpretation of experimental data.

This paper is organized in the following manner. First, model capabilities of simulating SHS of TiC is illustrated and discussed in detail from the kinetic point of view by presenting selected numerical simulation results based on the model outlined in Part I.[4] Then, model reliability is tested by comparison with suitable experimental data being nucleation parameters adopted for the fitting procedure. It should be noted that, apart from the ones related to nucleation processes, all thermodynamic and kinetic parameters have been taken from available literature sources. As explained in detail in the following sections, a best-fitting procedure on experimental data obtained from suitably executed experiments is adopted to quantify the values of the undetermined parameters.

Address all correspondence to these authors.
[a]e-mail: cincotti@visnu.disc.unica.it
[b]e-mail: cao@visnu.dicm.unica.it
DOI: 10.1557/JMR.2005.0153

II. NUMERICAL SOLUTION AND MODEL OUTCOMES

Model equations as well as theoretical details are reported in a companion paper;[4] parameter values used for the computations are summarized in Tables I and II where the corresponding literature sources are also quoted. Some of the thermodynamic quantities are indicated in the phase diagram reported in Fig. 2 of Part I.[4] The only parameters not readily available in the literature for the Ti–C system are the pre-exponential factor of nucleation B_0 and the interfacial energy between liquid Ti and solid TiC γ. Thus, in the following discussion, the latter ones, which are related to the nucleation phenomenon [see Eqs. (7)–(9) of Part I[4]], are considered the adjustable parameters of the proposed model. Refer to Nomenclature and Appendix sections of Part I [4] for the meaning of all reported symbols.

TABLE I. Values of physico-chemical parameters used during numerical simulations and corresponding literature reference (for symbols significance, see Ref. 4).

Symbol	Value	Unit	Reference
$Cp_{Ti}^{(\alpha)}$	…[a]	J kg^{-1} K^{-1}	13
$Cp_{Ti}^{(\beta)}$	…[a]	J kg^{-1} K^{-1}	13
$Cp_{Ti}^{(liq)}$	…[a]	J kg^{-1} K^{-1}	13
$Cp_{C}^{(s)}$	…[a]	J kg^{-1} K^{-1}	13
$Cp_{TiC}^{(s)}$	…[a]	J kg^{-1} K^{-1}	13
$Cp_{Diluent}^{(s)}$ (ZrC)	…[a]	J kg^{-1} K^{-1}	13
$Cp^{(gas)}$ (Argon)	…[a]	J kg^{-1} K^{-1}	13
D	…[a]	m^2 s^{-1}	14
E_D	78,000	J mol^{-1}	14
h	0	J s^{-1} m^{-2} K^{-1}	This work
H_{Ti}^0	0	J kg^{-1}	13
H_C^0	0	J kg^{-1}	13
H_{TiC}^0	−3,080,000	J kg^{-1}	13
H_D^0 (ZrC)	−1,905,000	J kg^{-1}	13
$H^{(gas),0}$ (Argon)	0	J kg^{-1}	13
$k_{Ti}^{(liq)}$	…[a]	W m^{-1} K^{-1}	15
$k_{Ti}^{(s)}$	…[a]	W m^{-1} K^{-1}	16
$k_C^{(liq)}$	$=k_C^{(s)}$	W m^{-1} K^{-1}	This work
$k_C^{(s)}$	…[a]	W m^{-1} K^{-1}	17
$k_{TiC}^{(s)}$	…[a]	W m^{-1} K^{-1}	18
$k_{Diluent}^{(s)}$ (ZrC)	…[a]	W m^{-1} K^{-1}	19
$k^{(gas)}$ (Argon)	…[a]	W m^{-1} K^{-1}	20
M_{Ti}	0.047867	kg mol^{-1}	16
M_C	0.0120107	kg mol^{-1}	16
M_{TiC}	0.0598777	kg mol^{-1}	16
$M_{Diluent}$ (ZrC)	0.1032347	kg mol^{-1}	16
$M^{(gas)}$ (Argon)	0.039948	kg mol^{-1}	16
l_{pore}^0	0	m	This work
N_A	6.022×10^{23}	mol^{-1}	16
P	0	Pa	This work
R	8.314	J mol^{-1} K^{-1}	16
t_{ig}	5	s	This work
T_0	298.15	K	This work
$\epsilon_{Ti}^{(s)}$	…[a]	…	21
$\epsilon_C^{(s)}$	…[a]	…	21
$\epsilon_{TiC}^{(s)}$	…[a]	…	22
$\epsilon_{Diluent}^{(s)}$ (ZrC)	…[a]	…	22
$\lambda_{m,Ti}$	236,000	J kg^{-1}	13
$\lambda_{t,Ti}$	70,000	J kg^{-1}	13
$\rho_{Ti}^{(liq)}$	4110	kg m^{-3}	14
$\rho_{Ti}^{(s)}$	4500	kg m^{-3}	16
$\rho_C^{(s)}$	2200	kg m^{-3}	16
$\rho_{TiC}^{(s)}$	4930	kg m^{-3}	16
$\rho_{Diluent}^{(s)}$ (ZrC)	6730	kg m^{-3}	16
σ	5.67×10^{-8}	W m^{-2} K^{-4}	16

[a]The corresponding values have been obtained by interpolating the data reported in the reference.

TABLE II. Values of physico-chemical parameters used during numerical simulations of ignition and corresponding literature reference (for symbols significance, see Ref. 4).

Symbol	Value	Unit	Reference
Cp_W	…[a]	J kg^{-1} K^{-1}	13
d_{coil}	0.016	m	This work
h	0	J s^{-1} m^{-2} K^{-1}	This work
h_{coil}	0.001	m	This work
L_{coil}	0.0617	m	This work
R_0	1.2×10^{-9}	Ω m	This work
s_{coil}	7.854×10^{-4}	m^2	This work
t_{ig}	5	s	This work
T_0	298.15	K	This work
V_0	21	V	This work
ϵ_W	…[a]	…	16
ρ_W	19250	kg m^{-3}	19
σ	5.67×10^{-8}	W m^{-2}K^{-4}	16
ζ_W	…[a]	Ω m	16

[a]The corresponding values have been obtained by interpolating the data reported in the reference.

The resulting system of algebraic and partial differential equations has been solved by adopting a centered finite-difference scheme for the spatial derivative at the internal node points in the z direction. The so-called method of moments[23] has been used instead to solve population balance of the Eqs. (11)–(13).[4] The resulting system of time-dependent ordinary differential equations has been integrated by means of the standard numerical routine DIVPAG of the IMSL library. A uniform grid of about 1000 discretization points was generally kept during computations. No significant change in the obtained results was observed using higher values of the internal node points.

It is not easy to get a comprehensive view of model capabilities due to its relatively high degree of sophistication. All phenomena take place simultaneously, and the detailed description of modeling results is difficult and cumbersome. For these reasons, it is appropriate to focus the discussion on the most important aspects of modeling outcomes.

In this section, we discuss a case study to offer a brief survey of the basic capabilities of the model and provide a better insight into the fundamentals of the modeling approach. According to the existing literature,[24,25] in the cases where a homogeneous nucleation process occurs, the characteristic pre-exponential factor of the nucleation rate B_0 and the solid-liquid interfacial energy γ can be

estimated to be 7.88 10^{+34} $K^{-1}mol^{-1}s^{-1}$ and 0.9 J/m^2, respectively. These values have been used to simulate the combustion process. For the sake of clarity, the following analysis of the combustion process is carried out with reference to the most important mechanistic steps mentioned in the modeling outline.

Once the combustion process has been ignited, a high-temperature combustion front is formed, which propagates at a certain velocity along the pellet. To deal with a stationary combustion front that is not affected by ignition conditions, let us focus our attention on the time evolution of the reacting system at $z = L/2$ along the pellet axis. The local temperature T changes during the course of the combustion process are shown in Fig. 1. A gradual temperature increase takes place until the temperature of 1166 K is reached, at which according to the phase diagram, the crystalline hexagonal close-packed α-phase Ti undergoes a second-order phase transition to the body-centered-cubic β-phase. Correspondingly, a small temperature plateau is observed, as shown in detail in the lower inset of Fig. 1. In the upper inset of the same figure, the plateau in the local temperature profile corresponding to the melting transition of Ti at the temperature $T = 1939$ K is clearly marked. The high rate at which the melting process occurs can be easily observed from the abrupt decrease in the mass of solid Ti, $m_{Ti}^{(s)}$, and the corresponding increase of liquid Ti mass, $m_{Ti}^{(liq)}$, shown in Fig. 2, where both mass concentrations are reported as a function of time t.

As the melting of Ti occurs, the free available pores between solid particles are instantaneously filled, and the area density of intimate contact between the melt and C solid particles, $a_{C\rightarrow liq}$, is correspondingly increased from the initial, negligible value to a finite one, as reported in Fig. 3. It can be seen that a maximum is reached very nearly corresponding with the completion of melting.

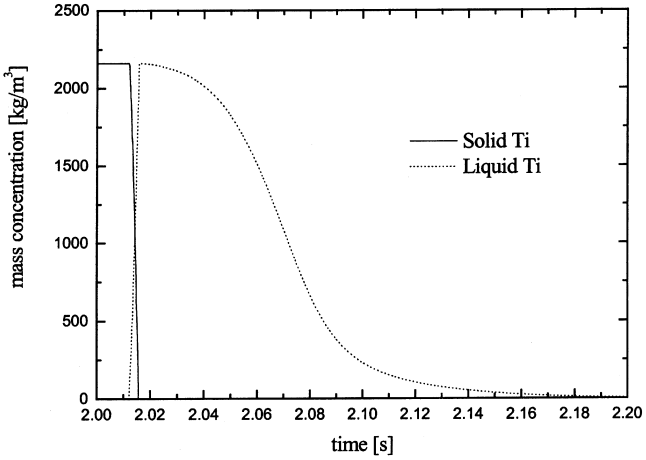

FIG. 2. Mass of solid and liquid reactant A as a function of time. $L = 0.04$ m; $D = 0.011$ m; $m_{Ti}^0 = 2161$ kg m^{-3}; $m_C^0 = 542$ kg m^{-3}; $m_{TiC}^0 = 0$ kg m^{-3}; $m_{Diluent}^0 = 0$ kg m^{-3}; $dp_{Ti}^0 = 22$ μm; $dp_C^0 = 1.5$ μm.

Under the action of the thermodynamic driving forces, the wetting of pores is accompanied by the dissolution of C into the molten Ti phase (see Fig. 4) and the formation of a Ti–C solution. As is evident from comparison between Figs. 3 and 4, the dissolution process starts as soon as liquid Ti and solid C come into contact. While melting takes place and the available pores are filled, the dissolution process occurs in parallel with the increase of the $Ti^{(liq)}$–$C^{(s)}$ intimate contact area density, $a_{C\rightarrow liq}$. However, the dissolution process determines the progressive reduction of the surface of spherical C particles, thus inducing a gradual decrease of the contact area (compare with Fig. 3).

The C content in the molten phase increases as a result of the dissolution process and reaches the thermodynamic solubility limit when the dissolution driving force Ω_D approaches zero (see Fig. 5). However, once the C content overcomes the thermodynamic limit for the

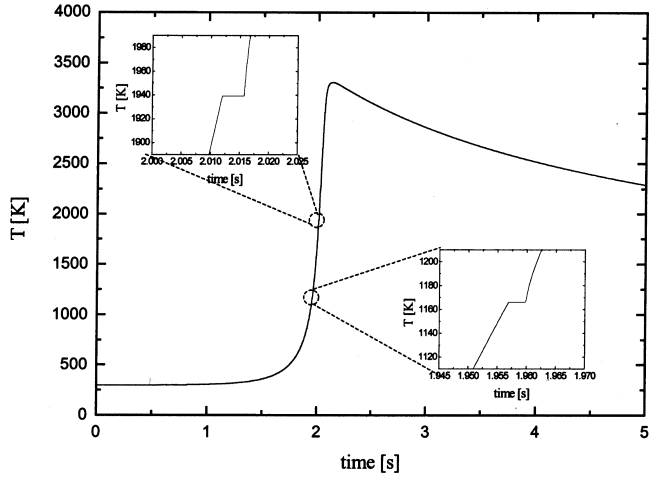

FIG. 1. Local temperature change as a function of time. $L = 0.04$ m; $D = 0.011$ m; $m_{Ti}^0 = 2161$ kg m^{-3}; $m_C^0 = 542$ kg m^{-3}; $m_{TiC}^0 = 0$ kg m^{-3}; $m_{Diluent}^0 = 0$ kg m^{-3}; $dp_{Ti}^0 = 22$ μm; $dp_C^0 = 1.5$ μm.

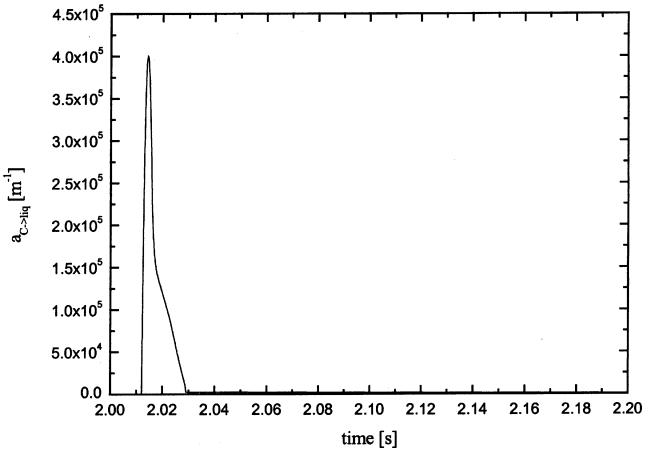

FIG. 3. Increase of the interfacial liquid-solid surface area as a function of time. $L = 0.04$ m; $D = 0.011$ m; $m_{Ti}^0 = 2161$ kg m^{-3}; $m_C^0 = 542$ kg m^{-3}; $m_{TiC}^0 = 0$ kg m^{-3}; $m_{Diluent}^0 = 0$ kg m^{-3}; $dp_{Ti}^0 = 22$ μm; $dp_C^0 = 1.5$ μm.

crystallization of TiC given by the TiC liquidus line on the left side of the phase diagram, the molten phase becomes supersaturated and the thermodynamic driving forces Ω_N and Ω_G, which determine nucleation and growth of solid TiC carbide, respectively, increase as clearly shown in Fig. 5. It is worth noting that the molten phase becomes supersaturated at times very close to the beginning of the dissolution process (i.e., Ω_N and Ω_G begin to increase right after Ω_D begins to decrease). This is certainly due to the low C content in the eutectic, as can be seen in the left part of the Ti–C phase diagram,[4] but also to the relatively high dissolution rate, as clearly confirmed by the rapid decrease to zero of Ω_D and the corresponding fast increase of Ω_N and Ω_G.

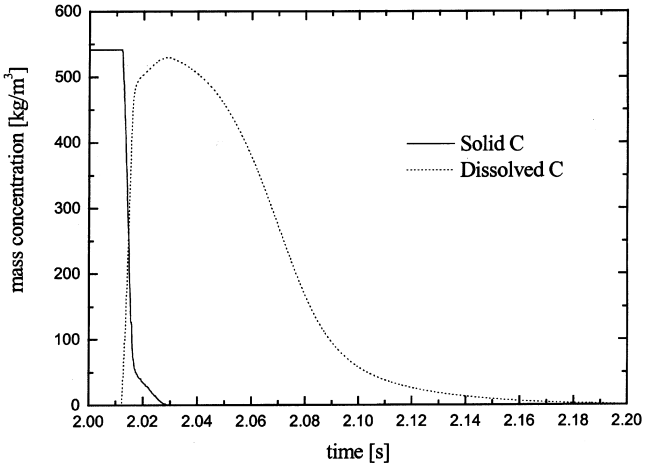

FIG. 4. Mass concentration of solid and dissolved C as a function of time. $L = 0.04\ m$; $D = 0.011\ m$; $m^0_{Ti} = 2161\ kg\ m^{-3}$; $m^0_C = 542\ kg\ m^{-3}$; $m^0_{TiC} = 0\ kg\ m^{-3}$; $m^0_{Diluent} = 0\ kg\ m^{-3}$; $dp^0_{Ti} = 22\ \mu m$; $dp^0_C = 1.5\ \mu m$.

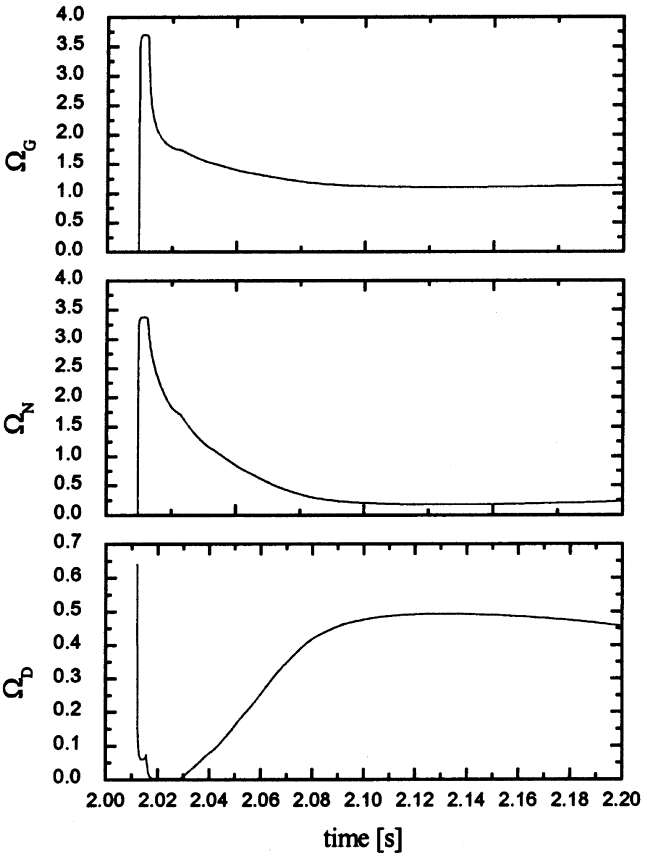

FIG. 5. Driving forces for dissolution, nucleation, and growth, respectively, as a function of time. $L = 0.04\ m$; $D = 0.011\ m$; $m^0_{Ti} = 2161\ kg\ m^{-3}$; $m^0_C = 542\ kg\ m^{-3}$; $m^0_{TiC} = 0\ kg\ m^{-3}$; $m^0_{Diluent} = 0\ kg\ m^{-3}$; $dp^0_{Ti} = 22\ \mu m$; $dp^0_C = 1.5\ \mu m$.

The sequence of simultaneous, co-related phenomena discussed above can be roughly summarized by superposing the temperature–composition curve related to the liquid phase on the phase diagram, as shown in Fig. 6. Even if in the figure all the detailed phenomena described above cannot be distinguished, this representation clarifies the important role played by dissolution on the whole SHS process. Indeed, the system rapidly moves toward the metastable extension of the liquidus curve of reactant C as a result of the relatively high dissolution rate. Afterwards, as the temperature increases, the C content in the molten phase follows the solubility line until the maximum value of x_C (i.e., the equiatomic composition of the initial reactants mixture) is reached. This value is maintained until the final total conversion is attained. Consequently, the rate of conversion seems to be mainly determined, at least in this case, by the rate of nucleation and growth. This system behavior explains that Ω_D starts increasing again after dropping to zero while both Ω_N and Ω_G reach maximum, as clearly depicted in Fig. 5.

The mass of solid TiC is quoted as a function of time in Fig. 7, in which it can be seen that nucleation and growth processes proceed at relatively higher rates under favorable conditions of high temperature as well as high degree of supersaturation. After an approximately exponential increase, the conversion of the initial Ti and C

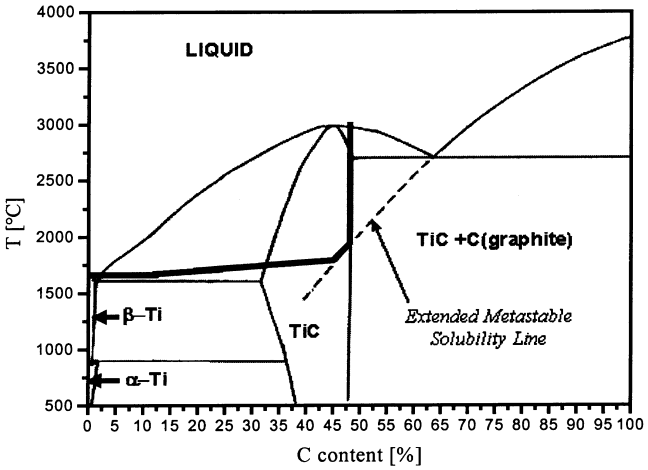

FIG. 6. (▬) System reacting path. $L = 0.04\ m$; $D = 0.011\ m$; $m^0_{Ti} = 2161\ kg\ m^{-3}$; $m^0_C = 542\ kg\ m^{-3}$; $m^0_{TiC} = 0\ kg\ m^{-3}$; $m^0_{Diluent} = 0\ kg\ m^{-3}$; $dp^0_{Ti} = 22\ \mu m$; $dp^0_C = 1.5\ \mu m$.

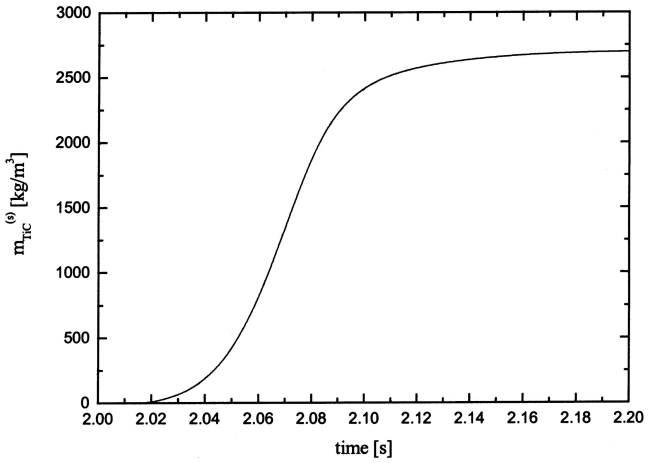

FIG. 7. Mass of solid TiC as a function of time. $L = 0.04\ m$; $D = 0.011\ m$; $m^0_{\mathrm{Ti}} = 2161$ kg m^{-3}; $m^0_{\mathrm{C}} = 542$ kg m^{-3}; $m^0_{\mathrm{TiC}} = 0$ kg m^{-3}; $m^0_{\mathrm{Diluent}} = 0$ kg m^{-3}; $dp^0_{\mathrm{Ti}} = 22$ μm; $dp^0_{\mathrm{C}} = 1.5$ μm.

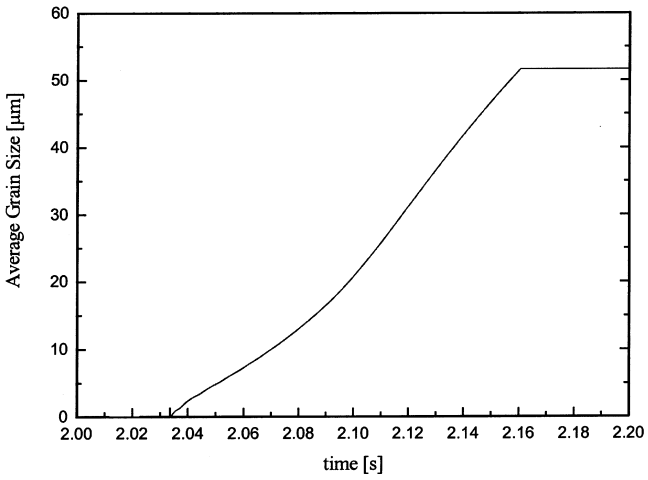

FIG. 9. Average grain size as a function of time. $L = 0.04\ m$; $D = 0.011\ m$; $m^0_{\mathrm{Ti}} = 2161$ kg m^{-3}; $m^0_{\mathrm{C}} = 542$ kg m^{-3}; $m^0_{\mathrm{TiC}} = 0$ kg m^{-3}; $m^0_{\mathrm{Diluent}} = 0$ kg m^{-3}; $dp^0_{\mathrm{Ti}} = 22$ μm; $dp^0_{\mathrm{C}} = 1.5$ μm.

reactants to the final product TiC is completed in about 0.2 s from the melting of Ti.

The normalized grain size distribution of TiC phase

$$n^* = n(t,r) \Big/ \int_0^\infty n(t,r)\mathrm{d}r,$$

is reported in Fig. 8 for different times. A typical Gaussian-like distribution develops after relatively short times. As expected, the grain growth process induces the gradual shift of the distribution toward larger particle sizes. The average grain size is reported in Fig. 9 as a function of time.

Modeling results reported above clearly point out the capability of the modeling approach to provide a detailed description of the combustion process in connection with the basic thermodynamic and kinetic properties of the Ti–C system. A variety of microscopic scale phenomena are shown to determine the whole combustion behavior. However, due to the experimental difficulties connected with the characterization of the combustion mechanism on the microscopic scale, only the usual macroscopic quantities of SHS processes, i.e., temperature profiles and propagation rates, are typically used to carry out a comparison with existing experimental data.

To this aim, the temperature profile along the pellet at a certain time t after ignition is shown in Fig. 10. As evident from the figure, a maximum combustion temperature of 3300 K is reached within the combustion front region. The position of the combustion front, represented by the location where the mixture reaches the 50% conversion along the z axis, is reported as a function of time in Fig. 11. Conversion is defined as $(m_C - m^0_C)/m^0_A + m^0_B)$ A relatively short period (about 0.5 s) is

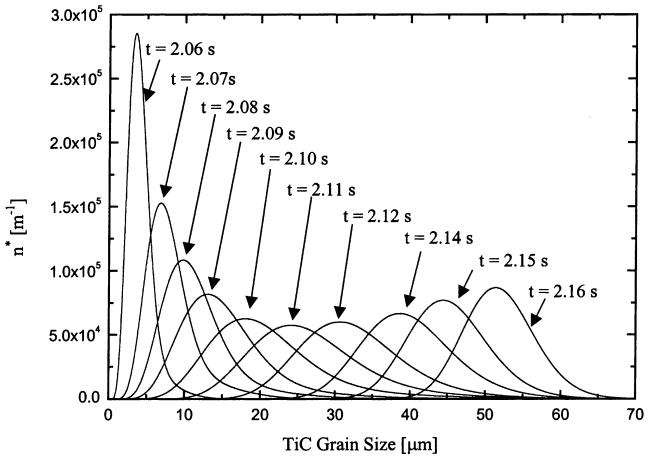

FIG. 8. Normalized grain size distributions at different times. $L = 0.04\ m$; $D = 0.011\ m$; $m^0_{\mathrm{Ti}} = 2161$ kg m^{-3}; $m^0_{\mathrm{C}} = 542$ kg m^{-3}; $m^0_{\mathrm{TiC}} = 0$ kg m^{-3}; $m^0_{\mathrm{Diluent}} = 0$ kg m^{-3}; $dp^0_{\mathrm{Ti}} = 22$ μm; $dp^0_{\mathrm{C}} = 1.5$ μm.

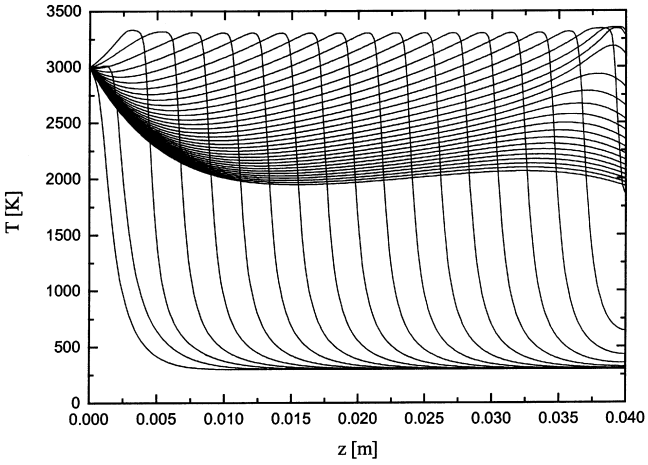

FIG. 10. Temperature profile along the pellet axis. $L = 0.04\ m$; $D = 0.011\ m$; $m^0_{\mathrm{Ti}} = 2161$ kg m^{-3}; $m^0_{\mathrm{C}} = 542$ kg m^{-3}; $m^0_{\mathrm{TiC}} = 0$ kg m^{-3}; $m^0_{\mathrm{Diluent}} = 0$ kg m^{-3}; $dp^0_{\mathrm{Ti}} = 22$ μm; $dp^0_{\mathrm{C}} = 1.5$ μm.

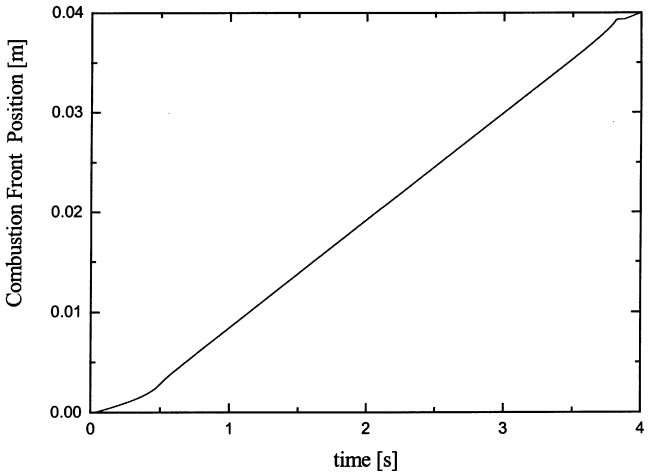

FIG. 11. Propagation rate along the pellet axis. $L = 0.04\ m$; $D = 0.011\ m$; $m^0_{Ti} = 2161$ kg m^{-3}; $m^0_C = 542$ kg m^{-3}; $m^0_{TiC} = 0$ kg m^{-3}; $m^0_{Diluent} = 0$ kg m^{-3}; $dp^0_{Ti} = 22\ \mu m$; $dp^0_C = 1.5\ \mu m$.

required for the system to reach a propagation mode characterized by a constant velocity equal to about 0.01 m s^{-1}.

Thus, the maximum combustion temperature and combustion front velocity at different process conditions, such as diluent content in the initial mixture, can be used to validate the proposed model by comparison with a suitable set of experimental data obtained, as discussed in Sec. III.

III. EXPERIMENTAL INVESTIGATION

Experimental runs were carried out with high-purity Ti (AEE, Bergenfield, NJ, <20 μm, purity 99.7%) and graphite (Sigma-Aldrich, Milano, Italy, 1–2 μm, synthetic) powders. It should be noted that such a choice of this graphite particle size is consistent with the previously assumed reaction mechanism. The Ti and C powders were then dry mechanically blended in a Spex Mixer model 8000 (Spex, Metachen, NJ) to form a homogenized mixture with equiatomic composition. Finally, the powder mixture was subjected to a pressure load of about 250 MPa in a hydraulic press (RMU M059, RMU, Reggio Emilia, Italy) to obtain a cylindrical pellet with a diameter of 0.011 m, a height of 0.04 m, and a density of about 2700 kg m^{-3}.

The cylindrical pellet was then placed inside the SHS reactor (see Cincotti et al.[26] for experimental apparatus details) to have its upper surface at about 1 mm from the W ignition coil (R.D. Mathis, Long Beach, CA, 0.04 W). The SHS reactor was sealed and evacuated down to about 1 Pa. Powders were then subjected to thermal ignition by allowing for the passage of electric current at 200 A and 20 V in the W coil for time intervals between 1 and 5 s. Temperatures and propagation rates of the reaction front were measured by means of a pyrometer (Ircon Mirage OR15-990, Ircon, Niles, IL) and a video camera (JVC, TK-1280E, JVC, Wayne, NJ).

Composition and crystallite size of the final products were determined by wide angle x-ray scattering (WAXS) with a Philips PW1830 diffractometer (Philips, Almelo, The Netherlands) equipped with CuK_α radiation tube. In particular, crystallite size of TiC product was obtained by the Rietveld method.[27]

SHS experiments were performed on $Ti_{50}C_{50}$ powder mixtures diluted with an inert phase content ranging from 0 to 20 wt% of high-purity ZrC (Alfa Aesar, Karlsruhe, Germany, −325 mesh, purity 99.5%) powders. This choice was due to the high melting temperature of the refractory compound and to the position of the characteristic diffractometric lines. The use of the ZrC compound allows, indeed, the clear detection of the lines of the TiC product phase, avoiding any superposition of the respective WAXS reflections. Figure 12 shows the x-ray diffraction (XRD) patterns of the product obtained when the ZrC content was 20 wt%. It is seen that the conversion of the initial reactants to the desired phase TiC is complete, as proven by the XRD analysis, which reveals the presence of TiC and ZrC only, and that the potential formation of solid solution between TiC and ZrC may be excluded.

IV. COMPARISON BETWEEN MODEL RESULTS AND EXPERIMENTAL DATA

To validate the model, the comparison against experimental data is reported in Figs. 13 and 14 in terms of combustion front velocity and maximum temperature, respectively, at various diluent content (weight percent ZrC). Even if the comparison is not satisfactory when adopting the values of B_0 and γ (i.e., $B_0 = 7.88\ 10^{34}$

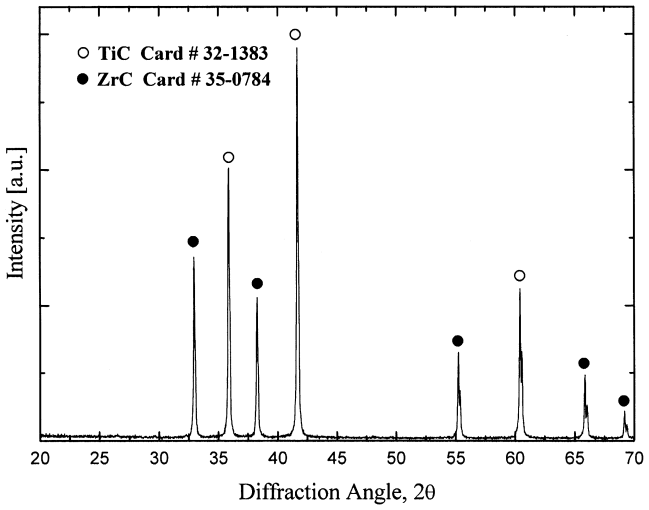

FIG. 12. XRD pattern of SHS product. $L = 0.04\ m$; $D = 0.011\ m$; $m^0_{Ti} = 2161$ kg m^{-3}; $m^0_C = 542$ kg m^{-3}; $m^0_{TiC} = 0$ kg m^{-3}; $m^0_{Diluent} = 593$ kg m^{-3}.

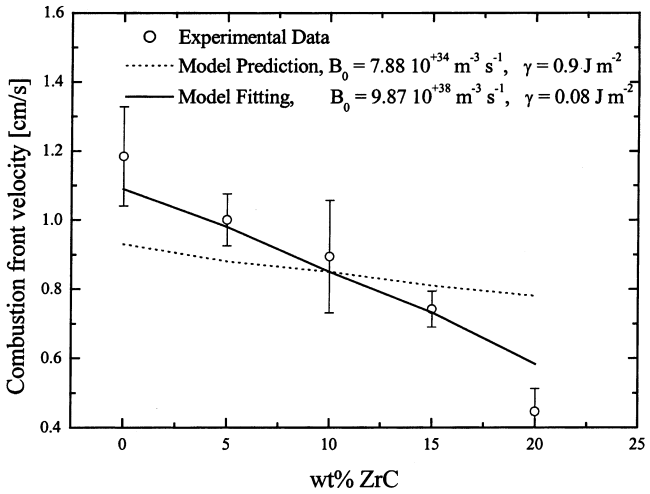

FIG. 13. Comparison between experimental data and model prediction results in terms of combustion front velocity. $L = 0.04$ m; $D = 0.011$ m; $m^0_{Ti} = 1897 \div 2161$ kg m^{-3}; $m^0_C = 476 \div 542$ kg m^{-3}; $m^0_{TiC} = 0$ kg m^{-3}; $m^0_{Diluent} = 0 \div 593$ kg m^{-3}; $dp^0_{Ti} = 22$ μm; $dp^0_C = 1.5$ μm; $dp^0_{Diluent} = 22$ μm.

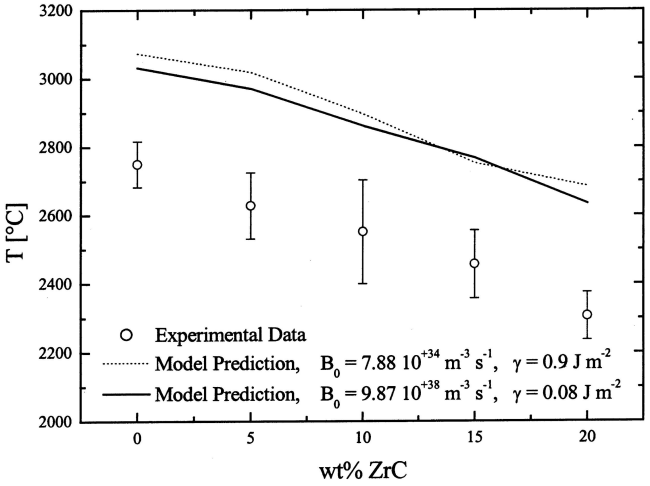

FIG. 14. Comparison between experimental data and model prediction results in terms of maximum combustion temperature. $L = 0.04$ m; $D = 0.011$ m; $m^0_{Ti} = 1897 \div 2161$ kg m^{-3}; $m^0_C = 476 \div 542$ kg m^{-3}; $m^0_{TiC} = 0$ kg m^{-3}; $m^0_{Diluent} = 0 \div 593$ kg m^{-3}; $dp^0_{Ti} = 22$ μm; $dp^0_C = 1.5$ μm; $dp^0_{Diluent} = 22$ μm.

$K^{-1}mol^{-1}s^{-1}$ and $\gamma = 0.9$ J/m^2, respectively) estimated from the literature, it is worth noting that model results may be regarded as predictions of the experimental behavior since no fitting procedure has been adopted.

It seems reasonable to ascribe the discrepancy obtained between model results and experimental data to the homogeneous nucleation parameters assumed so far, since heterogeneous nucleation is much more likely to take place in a porous system like a pellet of reacting powders. Therefore, the effective values of B_0 and γ may be evaluated by a fitting procedure.

The latter has been carried out against the experimental values of the propagation rate. In fact, previous numerical simulations performed to test model capabilities suggest that such a quantity is more sensitive to the rate of the nucleation process with respect to the maximum combustion temperature. The results of the best-fitting procedure are shown in Fig. 13. The obtained values of the parameters γ and B_0 were 0.08 J m^{-2} and 9.87 10^{38} m^{-3} s^{-1}, respectively.

The latter values are significantly different from the ones estimated for the case of a homogeneous nucleation process. The changing of B_0 cannot be easily related to reaction mechanism since, like any other pre-exponential factor, it strongly depends on the system investigated and the experimental condition considered such as the reactants powders characteristics. Conversely, the variation of the interfacial energy, which affects the activation energy [compare with Eq. (8) in Part I[4]], seems to confirm the occurrence of heterogeneous nucleation. In fact, it is well known that the latter phenomenon is characterized by smaller activation energies E_N; i.e., the γ values are generally lower than the ones associated with homogeneous nucleation processes.

The two parameter values obtained from the best-fitting procedure have been subsequently used to predict the trend followed by the maximum combustion temperature as a function of the ZrC content. Modeling results are reported in Fig. 14, together with the corresponding experimental data. It appears that nucleation parameters do not significantly affect the maximum combustion temperature. It is worth noting that the experimental temperature values invariably lie below the ones predicted by the model. Therefore, the model overestimates the maximum combustion temperature by about 200–300 K. A variety of factors can be cited to explain the observed discrepancy. However, at least three different aspects deserve a detailed explanation.

First of all, it is important here to underline the difficulty of obtaining a precise measurement of the maximum combustion temperature. Due to the very high values reached during the course of the combustion process, the temperature cannot be measured by resorting to the usual thermocouples. Pyrometric sensors must be used. However, their performances can be strongly affected by several factors. Volatilization of impurities ("self-cleaning effect") may reduce the pyrometer detection of emittance from reacting pellet by infrared adsorption. Moreover, actual emissivity of radiant surfaces may change during conversion from reactants to the final product and as a function of temperature while a single constant value was set into the pyrometer during experimental runs. Finally, it is worth noting that maximum combustion temperature are around 3000 °C, i.e., very close to the upper limit of operating range for the used pyrometer (i.e., 1000–3000 °C).

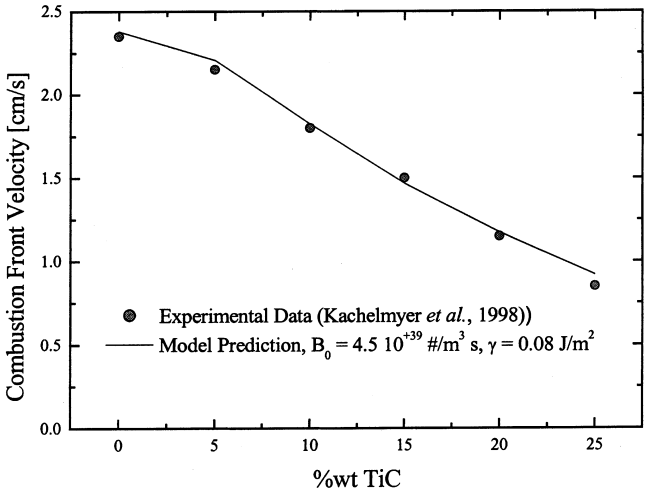

FIG. 15. Comparison between experimental data and model fitting results in terms of combustion front velocity. $L = 0.0275\ m$; $D = 0.0175\ m$; $m^0_{Ti} = 1197 \div 1500$ kg m^{-3}; $m^0_C = 300 \div 376$ kg m^{-3}; $m^0_{TiC} = 0 \div 499$ kg m^{-3}; $m^0_{Diluent} = 0$ kg m^{-3}; $dp^0_{Ti} = 22\ \mu m$; $dp^0_C = 0.5\ \mu m$; $dp^0_{TiC} = 22\ \mu m$.

Together with the difficulty of performing accurate measurements of the maximum combustion temperature, it is also important to underline a further aspect related to the use of the product enthalpy of formation values H^0_{TiC}. Model predictions have been carried out by employing a H^0_{TiC} value equal to 184.5 kJ mol^{-1}.[13] However, values reported in the literature cover a wide range between 129.6[28] and 230 kJ mol^{-1}.[29] Because model prediction is indeed extremely sensitive to the H^0_{TiC} value used, its choice is of fundamental importance to correctly reproduce the experimental trend of maximum combustion temperatures.

The model capability to correctly and effectively simulate heat losses is also briefly discussed, since during SHS wave propagation radial temperature gradients can be significant. It is well known that for a very high exothermic reaction, temperature gradients are confined in the outer region of the cross section of the reacting pellet. Thus, since using the pyrometer used during experimental investigation lateral surface temperature is being measured, a two-dimensional model would have been required for a more reliable comparison with experimental data. Thus, the discrepancies among measured and predicted values of the maximum combustion temperature may be then reasonably due to previous dissertations.

Next, as shown in Fig. 15, an experimental data set taken from the existing literature[30] has been simulated using the proposed model by consistently adopting the previously fitted value of the solid-liquid interfacial energy γ and suitably fitting the one corresponding to the pre-exponential factor B_0. These results represent, then, further support for the hypothesis that a heterogeneous nucleation process occurs during the course of the combustion reaction. It should be noted that the choice of this fitting procedure is related to the expected stronger dependence of reactant powder characteristics on B_0 than γ. The latter, indeed, can be considered specific to the TiC chemical system.

Model prediction has been tested even in terms of grain size of the reaction product TiC. The obtained results did not show satisfactory agreement with the corresponding experimental data. A possible reason for this discrepancy can be related to the assumptions associated to the growth rate mentioned in the paper devoted to the theoretical development of the proposed model.[4]

V. CONCLUDING REMARKS

The modeling approach developed along the line originally marked by Stangle and co-workers[10–12] permits a detailed description of the fundamental structural, thermodynamic, and kinetic features of SHS combustion processes. Taking into account the different phenomena simultaneously occurring during the course of the combustion reaction, the model allows for overcoming, at least partially, the well-known limitations associated with the representation of SHS phenomenology in terms of homogeneous or quasi-homogeneous processes.

In fact, in this work, the usual macroscopic quantities, such as front propagation velocity and maximum combustion temperature, as well as microstructural evolution of the final product, are explicitly connected with a sequence of elementary phenomena at the microscopic scale, i.e., phase transitions, dissolution, and crystallization.

The complex picture emerging as a result of the model sophistication permits to clarify some aspects of the SHS reactivity of the Ti–C system. By assuming that the melting of Ti is a necessary step to ignite the reaction, the formation of a molten phase induces the subsequent dissolution of the graphite. These processes are relatively fast, so the melt is rapidly supersaturated, and the rate of conversion is essentially determined by the rate of nucleation and growth. Moreover, comparison between model results and experimental data seems to confirm the occurrence of heterogeneous nucleation in product crystallization.

However, to achieve a complete and satisfactory comparison between modeling results and experimentally determined average grain size, the so-called "hard impingement" approach should be adopted to adequately describe the grain growth process. Work along these lines of inquiry is already underway, and separate papers will be devoted to specific improvements and developments.

ACKNOWLEDGMENT

The financial support of MIUR-PRIN (2002), Italy, Agenzia Spaziale Italiana (ASI), Italy, European Space

Agency (ESA) and NAMAMET (NMP3-CT-2004-001470), European Union (EU) is gratefully acknowledged.

REFERENCES

1. A. Varma, A.S. Rogachev, A.S. Mukasyan, and S. Hwang: Combustion synthesis of advanced materials: Principles and applications. *Adv. Chem. Eng.* **24,** 79 (1998).
2. J.J. Moore and H.J. Feng: Combustion synthesis of advanced materials: Part I. Reaction parameters. *Prog. Mater. Sci.* **39,** 243 (1995).
3. J.J. Moore and H.J. Feng: Combustion synthesis of advanced materials: Part II. Classification, application and modeling. *Prog. Mater. Sci.* **39,** 275 (1995).
4. A.M. Locci, A. Cincotti, F. Delogu, R. Orrù, and G. Cao: Combustion synthesis of metal carbides: Part I. Model development. *J. Mater. Res.* **20,** 1257 (2005).
5. A.M. Kanury: A kinetic model for metal + nonmetal reactions. *Metall. Trans.* **23A,** 2349 (1992).
6. A.K. Bhattacharya: Temperature enthalpy approach to the modeling of self-propagating combustion synthesis of materials. *J. Mater. Sci.* **27,** 3050 (1992).
7. E.A. Nekrasov, Y.M. Maksimov, and A.P. Aldushin: Mathematical model of combustion of a titanium-carbon system. *Combustion, Explosion, and Shock Waves* **17**(5), 513 (1981).
8. A. Makino: Fundamental aspects of the heterogeneous flame in the self-propagating high-temperature synthesis (SHS) process. *Prog. Energy Combust. Sci.* **27**(1), 1 (2001).
9. V.I. Yukhvid, S.V. Makladov, P.V. Zhirkov, V.A. Gorshkov, N.I. Timokhin, and A.Y. Dovzhenko: Combustion synthesis and structure formation in a model Cr–CrO_3 self-propagating high-temperature synthesis system. *J. Mater. Sci.* **32,** 1915 (1997).
10. Y. Zhang and G.C. Stangle: A micromechanistic model of the combustion synthesis process: Part I. Theoretical development. *J. Mater. Res.* **9,** 1994 (1994).
11. Y. Zhang and G.C. Stangle: A micromechanistic model of the combustion synthesis process: Part II. Numerical simulation. *J. Mater. Res.* **9,** 2605 (1994).
12. Y. Zhang and G.C. Stangle: A micromechanistic model of microstructure development during the combustion synthesis process. *J. Mater. Res.* **10,** 962 (1995).
13. I. Barin: *Thermochemical Data of Pure Substances* (VCH, New York, NY, 1993).
14. G.H. Geiger and D.R. Poirer: *Transport Phenomena in Metallurgy* (Addison-Wesley, Menlo Park, CA, 1973).
15. D.S. Viswanath and B.C. Mathur: Thermal conductivity of liquid metals and alloys. *Metall. Trans.* **3A,** 1769 (1972).
16. *CRC Handbook of Chemistry and Physics,* 80th ed., (CRC Press, Boca Raton, FL, 2000).
17. IIT Research Institute, *Handbook of Thermophysical Properties of Solid Materials* (Macmillan, New York, NY, 1961).
18. I.G. Korshunov, V.E. Zinov'ev, P.V. Gel'd, V.S. Chernyaev, A.S. Borukhovich, and G.P. Shveikin: Thermal diffusivity and thermal conductivity of titanium and zirconium carbides at high temperature. *High Temperature* **11,** 803 (1973).
19. *CRC Materials Science and Engineering Handbook,* 3rd ed. (CRC Press, Boca Raton, FL, 2001).
20. R.C. Reid, J.M. Prausnitz, and B.E. Poling: *The Properties of Gases and Liquids,* 4th ed., (McGraw-Hill, Singapore, 1988).
21. A. Sala: *Radiant Properties of Materials: Tables of Radiant Values for Black Body and Real Materials* (Elsevier, New York, NY, 1986).
22. *Handbook of High Temperature Compounds: Properties, Production, Applications,* edited by T.Ya. Kosolapova (Hemisphere, New York, NY, 1990).
23. H.M. Hulburt and S. Katz: Some problem in particle technology: A statistical mechanical formulation. *Chem. Eng. Sci.* **19,** 555 (1964).
24. J.A. Dirksen and T.A. Ring: Fundamental of crystallization: Kinetic effects on particle size distributions and morphology. *Chem. Eng. Sci.* **46,** 2389 (1991).
25. T. Nishizawa, I. Ohnuma, and K. Ishida: Correlation between interfacial energy and phase diagram in ceramic–metal systems. *J. Phase Equilib.* **22,** 269 (2000).
26. A. Cincotti, R. Licheri, A.M. Locci, R. Orrù, and G. Cao: A review on combustion synthesis of novel materials: Recent experimental and modeling results. *J. Chem. Technol. Biot.* **78,** 122 (2003).
27. L. Lutterotti and P. Scardi: Simultaneous structure and size-strain refinement by the Rietveld method. *J. Appl. Crystallogr.* **23**(4), 246 (1990).
28. D.L. Vrel, J.M. Lihrmann, and J.P. Petitet: Synthesis of titanium carbide by self-propagating powder reactions. 1. Enthalpy of formation of TiC. *J. Chem. Eng. Data* **40,** 280 (1995).
29. A.S. Mukasyan, A.S. Rogachev, and A. Varma: Mechanism of pulsating combustion during synthesis of advanced materials. *AIChE J.* **45,** 2580 (1999).
30. C.R. Kachelmyer, A. Varma, A.S. Rogachev, and A.E. Sytschev: Influence of reaction mixture porosity on the effective kinetics of gasless combustion synthesis. *Ind. Eng. Chem. Res.* **37**(6), 2246 (1998).